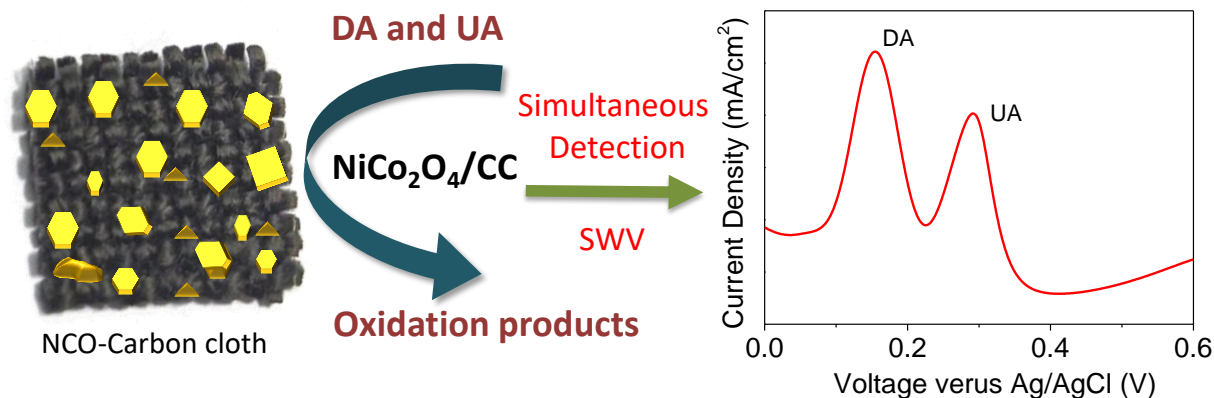


6

Biomolecular Sensing using Nickel Cobaltite Nanoplates

(Cited work: Urgunde et al., Chem.: Asian J, 2021 (DOI: 10.1002/asia.202101166))



6.1 Introduction

The human body fluids contain various biomolecules that are essential for motor and non-motor functions such as locomotion and cognition, and their monitoring can help in the screening of several diseases. In this context, dopamine (DA) is an essential neurotransmitter, and its changes in blood levels indicate various neurological disorders. Deficiency of DA can lead to disorders such as Parkinson's and Alzheimer's disease.[Huang et al., 2020a; Rajamani et al., 2018] Another important biomolecule is uric acid (UA), a product of purine metabolism and a biomarker for kidney diseases like gout and Lesch-Nyhan disease.[Alam et al., 2019] Low levels of UA can cause Wilson's disease, Fanconi syndrome, and Celiac disease.[Demirkan et al., 2020] Various analytical techniques such as high-performance liquid chromatography, colorimetric, electrochemical, and fluorescence have been used to detect these biomolecules simultaneously.[Jothi et al., 2018; Kretschy et al., 2012; Liu et al., 2018b; Peng et al., 2015] Compared to other methods, electrochemical methods have the advantages of high sensitivity, simple sample preparation, easy operation, quick response, and stable output.[Zhu et al., 2015a] The co-existence of several biomolecules in a physiological medium makes accurate detection difficult. Moreover, DA and UA biomolecules have a narrow range of detection potential. Hence to avoid false results, it is essential to detect DA and UA simultaneously.[Chambial et al., 2013] Electrochemical enzymatic biosensors have emerged as a promising analytical tool for real-time detection of such biomolecules because of their ease of usage, cost-effectiveness, versatility, compact design, portability, and reliable detection. There is surfeit literature related to the development of these electrochemical biosensors; however, the major drawback is enzymatic inhibition and degradation over time, resulting in false-positive outcomes. The enzymes have a short shelf-life, as they are sensitive to temperature, moisture, and other gases in the surroundings, which inhibit enzyme activity that decreases the sensor selectivity, affecting its sensitivity. Further, there are challenges associated with them, fouling, short response time, and overlapping of peak potentials, which can hinder the use of fabricated electrodes for simultaneous detection, thus making commercialization of electrodes a herculean task.[Jakubowska, 2011]

The electrodes for the electrochemical biosensing need to be highly efficient, rapid, and accurate in detecting DA and UA biomolecules. The sensitivity and performance can be enhanced by designing hybrid nanomaterials, doping, single-atom electrocatalyst,

functionalized microelectrodes, and the use of heterostructures. For example, Lu et al. synthesized covalent organic polymer-TiO₂/Ti₃C₂ heterostructure to detect DA and UA with LOD of 0.2 and 0.18 nM.[Taylor et al., 2019] Xie and group fabricated single-atom ruthenium biomimetic enzyme electrode supported on carbon nitride for simultaneous detection of DA and UA with LOD of 20 and 170 nM.[Xie et al., 2021] Nanocomposites of transition-metal-based oxides on carbon support such as ZnO-graphene,[Zhang et al., 2016b] NiO-graphene nanosheets,[Jahani et al., 2016] CuO-graphene,[Krishnamoorthy et al., 2018] and SnO₂-graphene[Rahman et al., 2017; Xie et al., 2015] have also been widely studied in literature due to their excellent properties like large surface area, porosity, high catalytic activity, fouling resistance, chemical, and mechanical stability, etc. However, metal oxide-based nanomaterials have issues related to the dissolution of metal ions, aggregation of nanoparticles, and Ostwald ripening, affecting their long-term stability despite their high performance. These problems can be addressed using spinel nanostructures with multiple metal ions as an electrocatalytic active material for simultaneous detection of biomolecules. Spinel nanostructures have been widely used in catalytic reactions due to their promising electrocatalytic activity, stability, and performance. Different spinels such as Fe₂O₃-GO,[Cai et al., 2019] Co₃O₄-GO,[Numan et al., 2017] N-Graphene nanosheets/CuCo₂O₄,[Tadayon et al., 2015] and NiFe₂O₄-activated carbon[Aparna et al., 2018] have been used in biomolecular sensing. For example, CuCo₂O₄ spinel nanoparticles supported on porous nitrogen-doped graphene nanosheets showed a LOD of 3.3, 4.9, and 4.1 μM for dopamine, melatonin, and tryptophan, respectively.[Tadayon et al., 2015] NiFe₂O₄-activated carbon on a glassy carbon electrode was used for DA detection with LOD of 1 μM.[Aparna et al., 2018] NiCo₂O₄ is an example of spinels used in the literature as a composite and hybrid material for biosensing applications. NiCo₂O₄ based nanocomposite have been used for the detection of biomolecules such as glucose,[Naik et al., 2017] trypsin,[Lin et al., 2018] pyridoxine,[Amini et al., 2020] 4-nitroquinoline N-oxide,[Chen et al., 2020] and urea.[Amin et al., 2019] The use of NiCo₂O₄ as an electrocatalyst for biosensing is limited due to the high resistance offered by the amorphous nanostructures and the use of binders/additives while fabricating the electrodes.

In this work, Co₃O₄, NiO, NiCo₂O₄ were prepared by solventless thermolysis of Co hexadecanethiolate (Co-HDT) and Ni butanethiolate (Ni-BT) inks and mixture (4:1) as reported in the previous chapter. The electrochemical properties of Co₃O₄, NiO, NiCo₂O₄ and the performance of the fabricated electrodes were studied using square wave voltammetry (SWV) towards DA and UA detection. NiCo₂O₄ nanoplates formed have single-crystalline nature, high conductivity, and an electrochemically active surface that allows easy interaction with various biomolecules. NiCo₂O₄/CC as a biosensor exhibit an excellent electrocatalytic activity with superior analytical parameters such as low detection limit, sensitivity, and wide range of detection with excellent sensitivity for biomolecular detection.

6.2 Objectives of the Work

The objectives of this work are as follows:

1. To fabricate NiO, Co₃O₄ and NiCo₂O₄/CC electrodes and test their performance towards electrochemical detection of dopamine and uric acid.
2. To test the electrodes by pulse voltametric techniques for biosensing application
3. calibrate the sensor for different concentrations of different biomolecules under optimized conditions.
4. To test the fabricated sensors for simultaneous detection in presence of various interfering ions for practical application.

6.3 Experimental

The Co-HDT and Ni-BT precursors were synthesized using general two-step process, detailed in Chapter 2, section 2.4.2.

6.3.1 Material Characterization

The morphology of the Ni-Co oxide-based samples was examined by field-emission scanning electron microscopy (FESEM) (Nova NanoSEM 600 instrument, FEI Co., The Netherlands). HRTEM and ED patterns were recorded using Talos 2000S G2 FEG with a beam energy of 200 kV. X-ray photoelectron spectroscopy (XPS) was carried out using Omicron Nanotechnology (Oxford Instruments). The XPS peaks were fitted with the vigot function using XPS Peak 4.1 software.

6.3.2 Electrochemical Characterization of Electrocatalyst

Conducting carbon cloth (CC) was purchased from Fuel Cell Earth LLC (Product Code CP40). The NCO-based electrodes were directly prepared by dip-coating CC substrate of 0.5 cm² in Ni-Co thiolates (5 mg/mL) five times with different molar ratios, following which it was thermolysed at 350°C in a nitrogen atmosphere for 3 hrs. The coating conditions were kept constant during all depositions for the sake of comparison of results. The electrochemical properties were studied on the electrochemical workstation (CHI 660E) in a three-electrode geometry containing an Ag/AgCl reference electrode and Pt as a counter electrode. The measurements were carried out in a solution of 0.1 M phosphate buffer (PBS) (pH = 7). The NCO/CC was used as the working electrode for the electrochemical measurements. Before electrochemical measurements, the electrodes were activated by carrying out 25 consecutive CV scans in 0.1 M PBS and a voltage range of -0.2 to 0.6 V versus Ag/AgCl till a stable overlapping response was obtained. The square wave voltammetry (SWV) was recorded in the voltage range of 0 to 0.6 V with an increment of 1 mV, frequency of 10 Hz, and pulse height of 30 mV versus Ag/AgCl. Electrochemical impedance spectroscopy (EIS) measurements were performed using an in-built impedance module of the workstation. Data were collected at 0.60 V in a frequency range from 0.1 Hz to 10 MHz and the potential amplitude of 10 mV. Chronoamperometry (I-t) measurements are performed at different voltages for studying the dynamic resonance of the sensor.

6.4 Results and Discussion

6.4.1 Fabrication of Co₃O₄/CC, NiO/CC and NiCo₂O₄/CC Electrodes

It is well-known in the literature that Ag and Cu alkane thiolates self-assemble to form supramolecular structures with lamellar and micellar phases that on decomposition can result in atomically thin sheets of metal nanostructures. Herein, we have synthesized Co₃O₄, NiO and NiCo₂O₄ using Co-HDT and Ni-BT inks as previously reported by our group for application as sensing platform for biosensing. The role of NiCo₂O₄ nanoplates as an efficient catalyst is elucidated in this work for the simultaneous detection of UA and DA as a biosensor.

Figure 6.1a shows the schematic demonstrating the synthesis method based on the mesoscopic assembly of mixed thiolate precursors followed by solventless decomposition resulting in thin nanoplate-like structures. Co₃O₄, NiO, and NiCo₂O₄ nanostructures were synthesized on carbon cloth (CC) substrate by thermolytic decomposition of Co-HDT, Ni-BT, and Co-HDT: Ni-BT (4:1) mixture, respectively, following the conditions detailed in the experimental section. The

structural purity and phase of oxides obtained after the thermolysis of Co-HDT, Ni-BT, and their 4:1 mixture was confirmed by XRD measurements (Figure 5.3b).

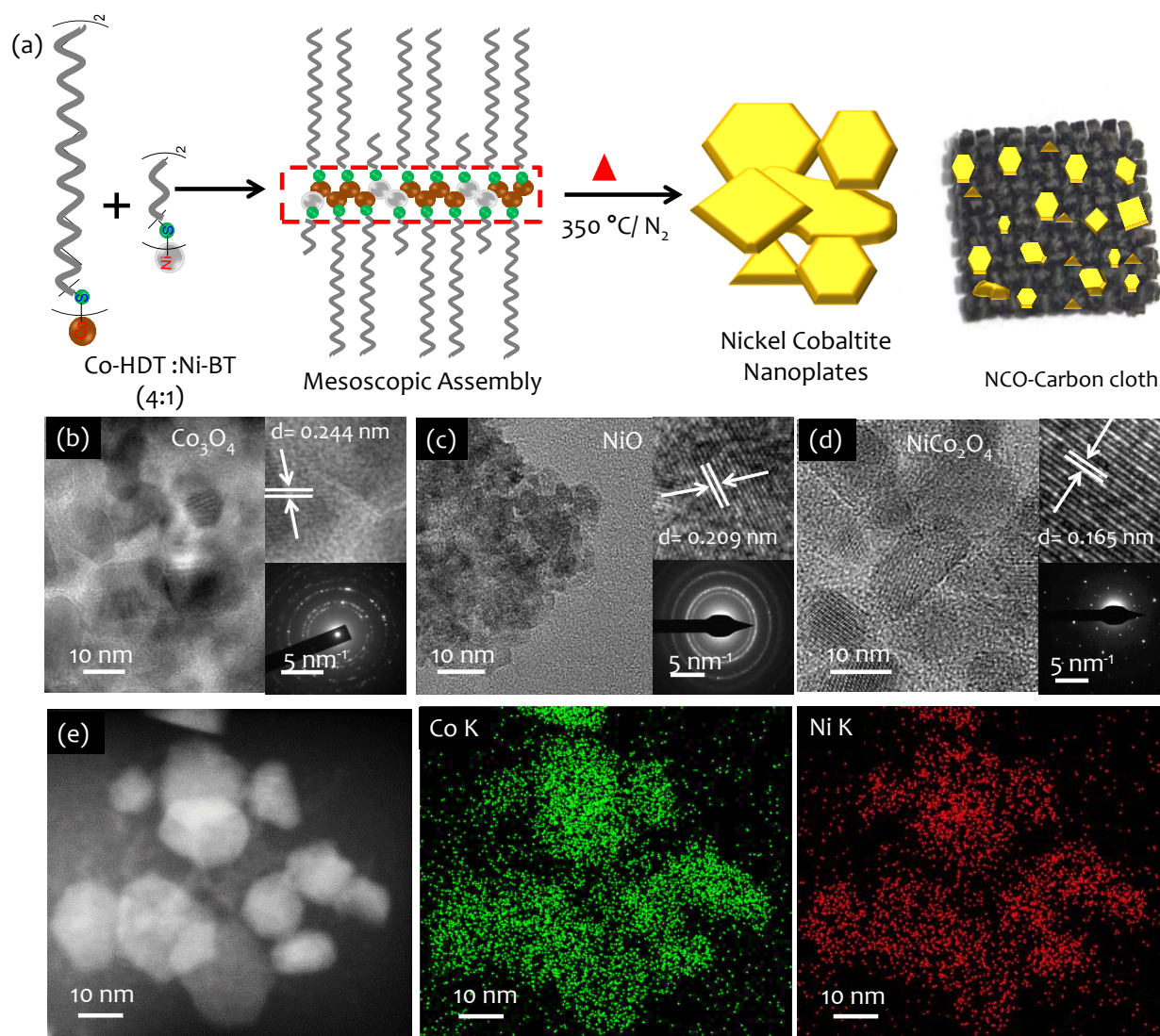


Figure 6.1: (a) Schematic demonstrating the NiCo₂O₄ nanoplates formation on carbon cloth substrate (b-d) High resolution TEM images with insets showing magnified images and Selected Area Electron Diffraction pattern of Co₃O₄, NiO, and NiCo₂O₄. (e) HAADF-STEM image and corresponding EDS maps of Co K-edge and Ni K-edge signals originating from NiCo₂O₄ nanoplates.

The XRD patterns of Co₃O₄ and NiCo₂O₄ resembled the polycrystalline cubic spinel structure, while NiO exhibits planes corresponding to face-centered cubic NiO without any impurity peaks. The structure and morphology are further characterized by HRTEM images and their corresponding ED patterns (Figure 6.1b-d). Co₃O₄ and NiO show well-resolved lattice planes corresponding to 311 (d-spacing of 2.44 Å) and 200 planes (2.09 Å), respectively (Figure 6.1b-c). The diffuse rings and sharp spots in the SAED pattern (Inset, Figure 6.1b-c) confirm the polycrystalline nature of Co₃O₄ and NiCo₂O₄. The synthesized NiCo₂O₄ shows the ultrathin and highly crystalline nanoplate-like structure with dominant 422 planes (d = 1.65 Å) of the spinel (Figure 6.1d). The hexagonally arranged sharp diffraction spots in the SAED pattern reaffirm the single-crystalline nature of NiCo₂O₄ nanoplates.

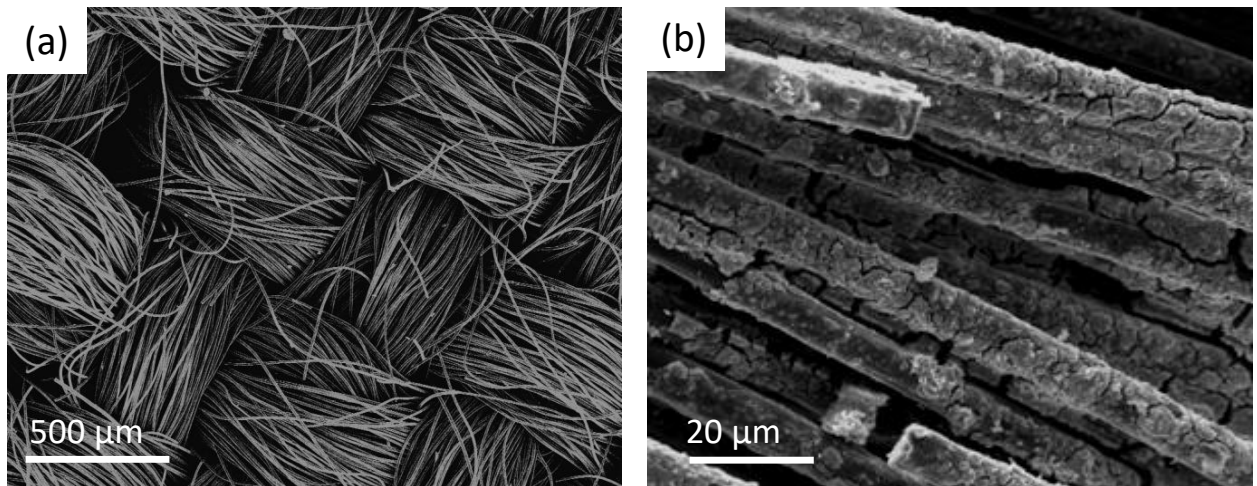


Figure 6.2: FESEM image of (a) carbon cloth coated with NiCo_2O_4 and corresponding (b) magnified image shows the dense film over carbon fibers.

The FESEM image shows the dense and uniform coating of NiCo_2O_4 on carbon cloth substrate obtained after dip coating making it ideal for biosensing application (Figure 6.2). The HAADF-STEM image and corresponding EDS mapping in Figure 6.1e show a uniform distribution of Ni and Co, emphasizing the fact that the formation of a solid solution of NiCo_2O_4 ultrathin nanoplates has taken place rather than phase segregated NiO and Co_3O_4 oxides.

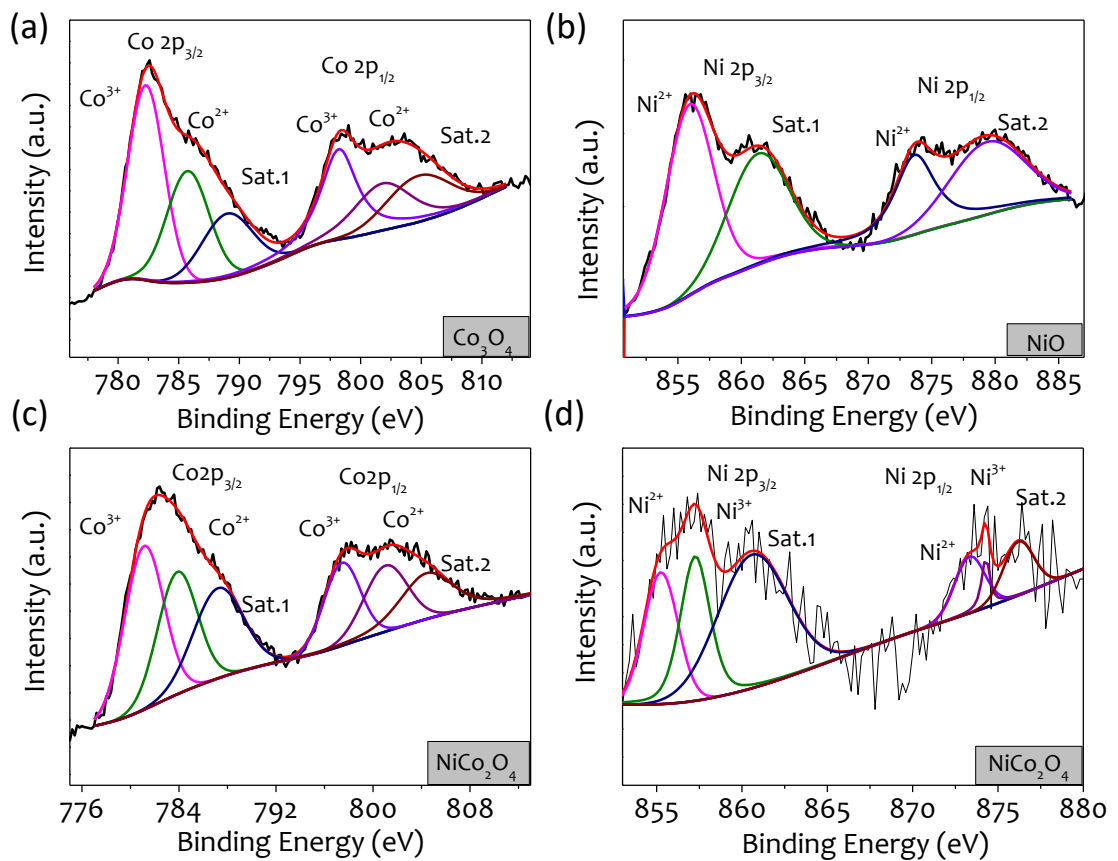


Figure 6.3: Deconvoluted XPS spectra of Co 2p and Ni 2p of (a) Co_3O_4 (b) NiO and (c-d) NiCo_2O_4 , respectively.

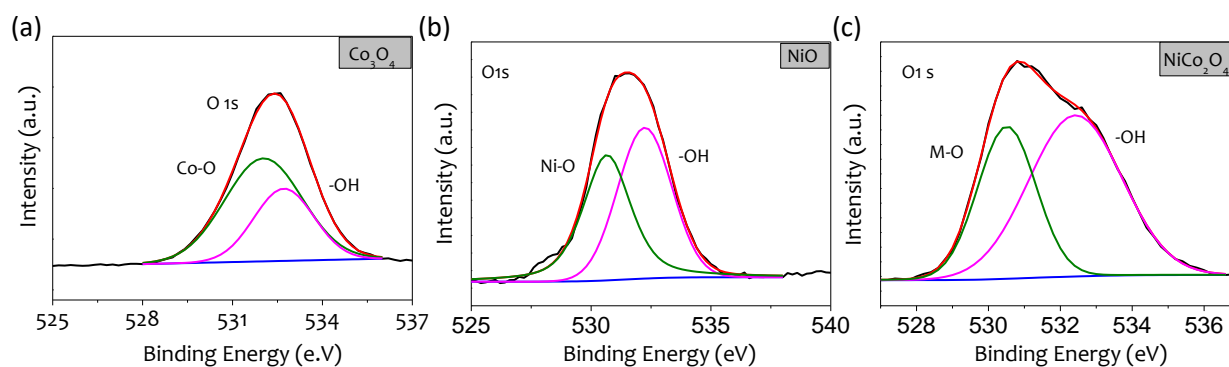


Figure 6.4: (a-c) High-resolution O 1s core level spectra of Co_3O_4 , NiO , and NiCo_2O_4 respectively.

Table 6.1: Binding Energy (BE) values derived from deconvoluted XPS spectra of Co 2p, Ni 2p, and O 1s.

No.	Ni (eV)						Co (eV)						O (eV)		
	Ni^{3+}		Ni^{2+}		Sat-1	Sat-2	Co^{3+}		Co^{2+}		Sat-1	Sat-2	Hydroxyl	Ni-O	Co-O
	$2p_{3/2}$	$2p_{1/2}$	$2p_{3/2}$	$2p_{1/2}$	$2p_{3/2}$	$2p_{1/2}$	$2p_{3/2}$	$2p_{1/2}$	$2p_{3/2}$	$2p_{1/2}$	$2p_{3/2}$	$2p_{1/2}$			
0	N.A.	N.A.	N.A.	N.A.	N.A.	N.A.	782.4	798.2	785.8	802.0	789.2	805.8	532.8	N.A.	532
20	857.2	876.4	855.2	874.2	860.6	873.4	781.2	797.6	784.0	801.2	787.2	804.4	532.4	530.6	
100	N.A.	N.A.	856.0	873.6	861.6	879.4	N.A.	N.A.	N.A.	N.A.	N.A.	N.A.	532.2	530.6	N.A.

N. A. indicates data not applicable

The oxidation states present on the surface play an essential role in the electrocatalytic activity. A detailed analysis of deconvoluted high-resolution XPS spectra of the NiO , Co_3O_4 , and NiCo_2O_4 is performed in Figure 6.3. The high-resolution spectra of O 1s of electrodes are provided in Figure 6.4. The O 1s peaks (Figure 6.4a-c) were deconvoluted into -OH, Ni-O, and Co-O. The -OH peak around 532 eV indicates surface hydroxylation, and the peak around 530 eV corresponds to the metal-oxygen bond from Ni-O or Co-O.[Chen et al., 2018a] The binding energy values are tabulated in Table 6.1. The Co 2p core-level XPS in Figure 6.3a fits well with two spin-orbit doublets corresponding to Co^{3+} and Co^{2+} along with the shake-up satellites, indicating the formation of Co_3O_4 . The $\text{Co}^{3+}/\text{Co}^{2+}$ ratio is 0.64, which is lower than the theoretically expected ratio of 2 due to the surface oxidation of Co^{2+} to Co^{3+} . The Ni 2p fitted to two spin-orbit doublets is characteristic of Ni^{2+} while two shake-up satellites at 861.6 and 879.4 eV correspond to NiO formation (Figure 6.3b).[Peck et al., 2012] A peak separation of ~17 eV in the spin-orbit coupling also confirms the formation of $\text{Ni}(\text{OH})_2$ on the NiO surface.[Urgunde et al., 2018] The Co 2p and Ni 2p spectra of the as-prepared NiCo_2O_4 samples are shown in Figure 6.3c and d, respectively. In Co 2p, the peaks corresponding to Co^{3+} and Co^{2+} , along with shake-up satellites, are also seen. The $\text{Co}^{3+}/\text{Co}^{2+}$ ratio of 0.95 is relatively close to the theoretical value of 1 in NiCo_2O_4 . The XPS spectra of Ni 2p show Ni^{3+} and Ni^{2+} oxidation states, unlike only Ni^{2+} in NiO. The presence of Ni^{3+} oxidation states on the surface indicates the formation of NiCo_2O_4 . From the above discussion, it can be concluded that Ni^{3+} , Ni^{2+} , Co^{3+} , and Co^{2+} are present as expected for NiCo_2O_4 . [Mahala et al., 2017; Wu et al., 2017a] It has been observed in the literature that the multiple oxidation states favor the electrochemical reactions; hence, superior electrochemical catalytic performance can be expected in NiCo_2O_4 for the presence of mixed valance states.[Li et al., 2011]

6.4.2 Electrochemical Performance of NiCo₂O₄/CC

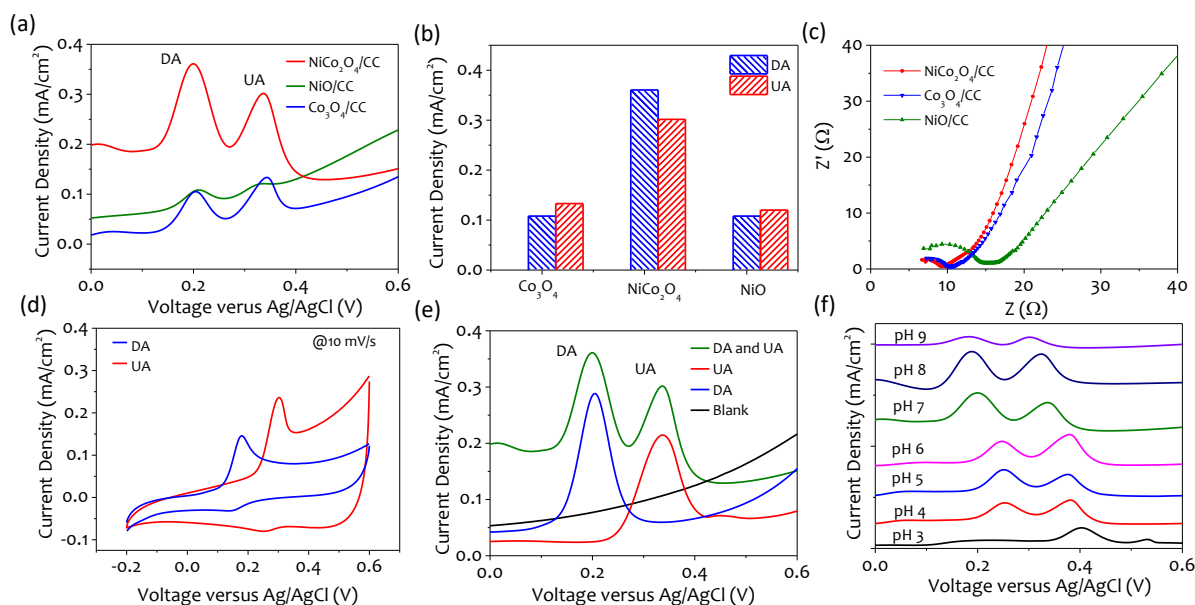


Figure 6.5: (a) Square Wave Voltammetry (SWV) of Co₃O₄/CC, NiO/CC and NiCo₂O₄/CC electrodes with 200 μM DA, 50 μM UA and mixture of DA (200 μM) and UA (50 μM) and corresponding (b) current response of electrodes for simultaneous detection of UA and DA. (c) EIS Nyquist plot of all electrodes. (d) CV at 10 mV/s and (e) SWV of NiCo₂O₄/CC with DA (200 μM) and UA (100 μM). The mixture of DA (200 μM) and UA (100 μM) is also included for simultaneous detection (f) Influence of electrolyte pH on oxidation peak potentials. (Note: y-scale is the same for all graphs and hidden for clarity).

The Square Wave Voltammetry (SWV) response of NiCo₂O₄ electrode is compared with Co₃O₄ and NiO for a mixture of 200 μM DA and 50 μM UA in 0.1 M PBS (pH). The SWV shows a relatively sharp and strong anodic peak toward the oxidation of DA and UA for NiCo₂O₄/CC than Co₃O₄/CC and NiO/CC. NiCo₂O₄/CC exhibits two well-defined voltammetric peaks at potentials 0.20 V and 0.34 V with a ~three times increase in peak current for DA and UA, assigned to the faster charge transfer rate of the NiCo₂O₄ spinel (Figure 6.5a-b). From the SWV current response, it can be concluded that NiCo₂O₄ achieves the best performance for simultaneous detection of 200 μM DA and 50 μM UA in terms of current density, indicating the intrinsic superiority of the NiCo₂O₄ nanoplates based electrode. The charge transport characteristics of three electrodes (Co₃O₄/CC, NiO/CC, and NiCo₂O₄/CC) were investigated using electrochemical impedance spectroscopy (EIS) over a frequency range of 0.1 - 1 MHz at an open-circuit voltage of 0.6 V versus Ag/AgCl in 0.1 M PBS. The interfacial charge transfer resistance (R_{ct}) values of these electrodes were obtained from the semicircular region shown in Figure 6.5c. The lowest R_{ct} value of NiCo₂O₄/CC (~9.30 Ω) indicates better electron transfer rate and electrocatalytic activity compared with Co₃O₄/CC (~10.31 Ω) and NiO/CC (~14.34 Ω). The enhanced electrochemical redox of DA and UA on NiCo₂O₄/CC can be ascribed to abundant surface active sites that favor adsorption of small biomolecules like DA and UA leading to the effective catalytic reaction of DA and UA. On the other hand, electron transfer between NiCo₂O₄/CC and the electrode surface was significantly facilitated due to the excellent conductivity of single-crystalline nanoplates and the synergistic effect of Ni and Co species with multiple oxidation states in NiCo₂O₄.

The CV measurements also exhibit well-defined pair of reversible redox peaks at 0.180 and 0.175 V (Figure 6.5d) due to oxidation of catechol in DA to o-quinone and vice versa (Figure 6.5d). [Kaur et al., 2015; Struck et al., 1965] The relative oxidation and reduction peak intensity differences demonstrate the excellent reversibility of DA on the NiCo₂O₄/CC. Since the ratio of oxidation peak and the reduction peak current is less than one, the reaction is quasi-reversible. In the case of UA, there appears a strong oxidation peak at 0.30 V and a tiny reduction peak at

0.24 V, indicating irreversibility of UA, unlike DA. The major by-product of UA oxidation in an aqueous medium is 4,5-dihydroxyluric acid which is unstable and decomposes to redox inactive, allantoin molecule.[Kaur et al., 2015]

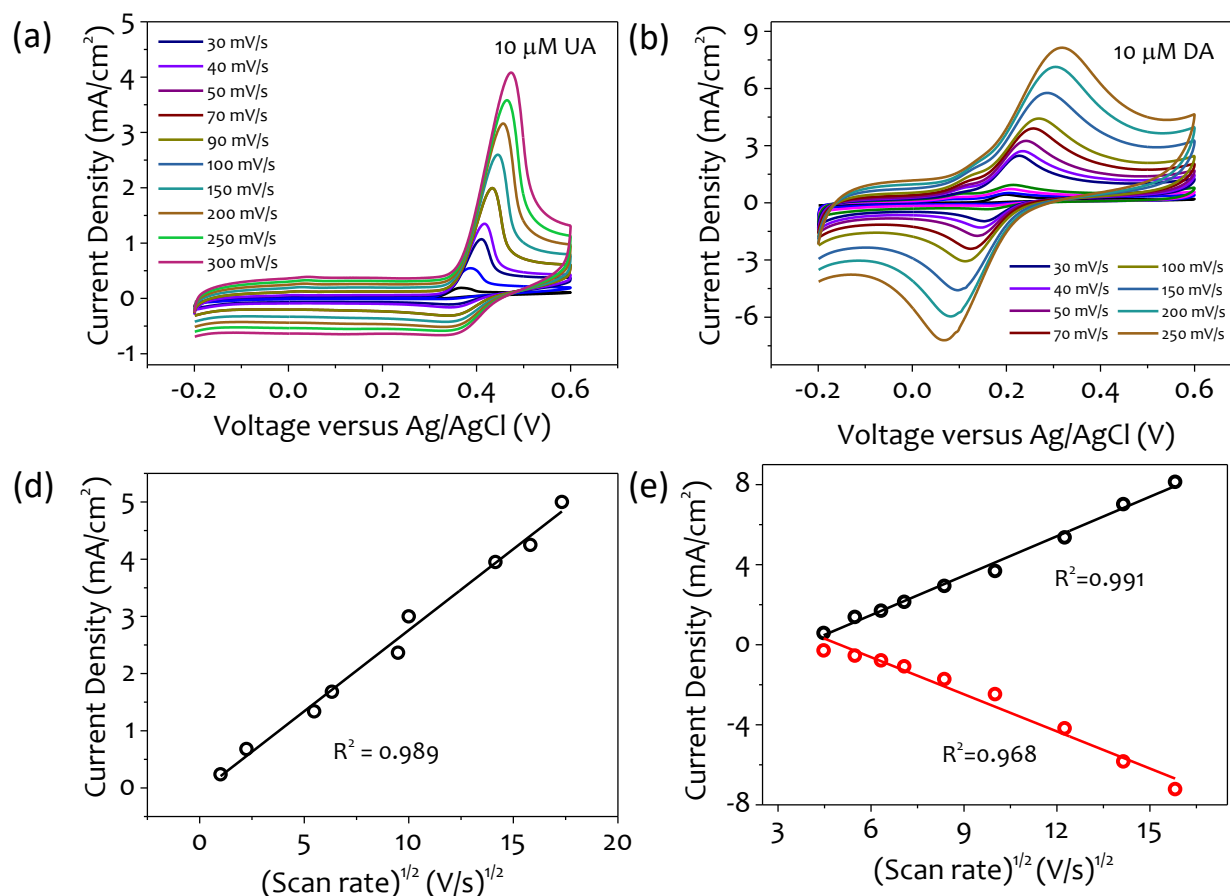


Figure 6.6: (a-b) CV of NiCo₂O₄/CC in 10 μM DA and 10 μM UA with varying scan rates (30-300 mV/s) and its (c-d) corresponding plot of current densities versus square root of scan rate, respectively.

The electrodes were subjected to increasing scan rates from 1-300 mV/s to study the kinetics of the oxidation process of DA and UA (Figure 6.6a and b). The peak current densities show linear dependence against the square root of scan rate, suggesting that oxidation of DA and UA are diffusion-controlled processes (Figure 6.6c and d). The excellent response of NiCo₂O₄/CC towards the oxidation of DA and UA is due to the enhanced catalytic activity of the Ni and Co atoms. The electrochemical response of NiCo₂O₄/CC towards DA and UA was further investigated using SWV (Figure 6.5e). On addition of 200 μM DA into PBS, a well-defined oxidation peak was observed at 0.2 V, while in the case of 100 μM UA, there appears a remarkable oxidation peak at 0.34 V due to the oxidation of UA. When UA and DA are introduced together, a significant separation of 140 mV in peak potentials (ΔE) is found, ensuring the possibility of simultaneous detection of both the biomolecules. Thus, it can be concluded that NiCo₂O₄/CC is an efficient electrode in the discrimination of DA and UA, and the determination of the biomolecules can be carried out even in mixtures. The performance of the NiCo₂O₄/CC towards the simultaneous detection of DA and UA is examined in different pH conditions (Figure 6.5f).

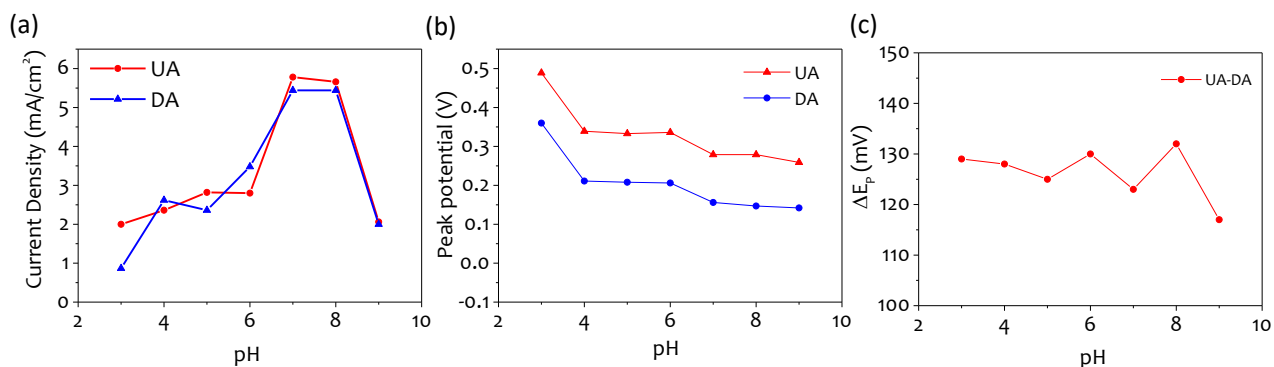


Figure 6.7: Variation in (a) peak current densities with pH, (b) peak potential with pH and (c) peak separation with pH in 50 μM DA and 200 μM UA.

The peak potentials for the oxidation of DA and UA are shifted at higher pH values, indicating that protons (H^+) formed in the electrocatalytic oxidation of DA and UA take part in the reaction processes. However, at low pH values, the high concentration of H^+ affects the electrocatalytic oxidation due to the common ion effect, resulting in a low voltammetric signal. [Kaur et al., 2015] The separation of peak potentials of NiCo_2O_4 for DA and UA increases with pH changing from 5.0 to 8.0. When the pH value decreases/increases to either 3 or 9, the response of DA and UA becomes poor. For the best performance, pH of 7 was selected as the optimal value of the PBS for further experiments, as shown in Figure 6.7. Moreover, it is also ideal for bio-environmental studies and suitable for DA and UA detection in any biological system.

6.4.3 Individual and Simultaneous Detection of DA and UA

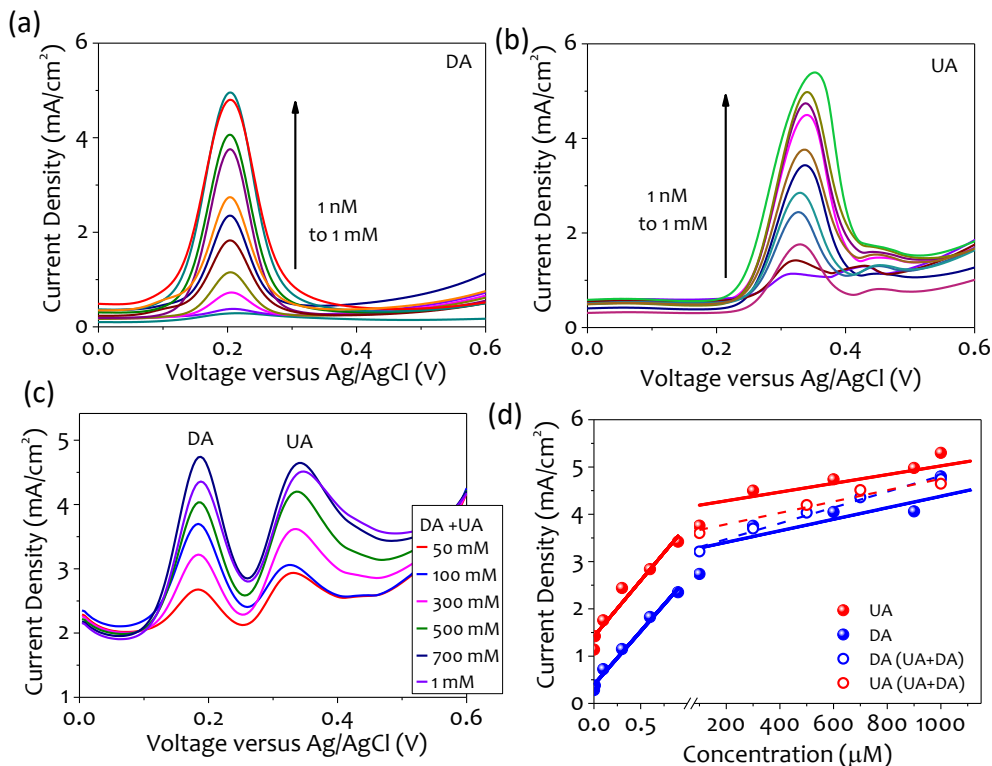


Figure 6.8: Square Wave Voltammograms (SWVs) of (a) DA and (b) UA from 1 nM – 1000 μM concentration, (c) simultaneous detection with increasing biomolecules (DA and UA respectively) and corresponding (d) calibration plots on $\text{NiCo}_2\text{O}_4/\text{CC}$.

The electrochemical performance of the NiCo₂O₄/CC was examined under the optimized conditions by SWV experiments as detailed in the experimental section.[Joshi et al., 2016] The SWV at different concentrations of DA and UA was performed individually on NiCo₂O₄/CC electrodes (Figure 6.8a and b). The peak current density increased when DA and UA concentrations were changed from 1 nM to 1000 μM, independently. The ability of NiCo₂O₄/CC electrode towards the simultaneous detection of UA and DA was investigated using SWV as the voltammograms obtained show considerably separate peak potentials. Hence, the possibility of determining the individual concentrations of these compounds from a mixed concentration of the biomolecules is explored in this study. Figure 6.8c displays the electrocatalytic oxidations of DA and UA on NiCo₂O₄/CC simultaneously with equimolar concentrations of both molecules. It can be observed that two well-defined voltammetric peaks corresponding to the oxidation of DA and UA, respectively, appear at NiCo₂O₄/CC, and the peak currents increased in proportion to the concentrations of DA and UA due to facile diffusion of DA and UA at NiCo₂O₄/CC electrode surface. The calibration curves for the individual and simultaneous detection of DA and UA are shown in Figure 6.8d. The calibration plot confirms that individual detection of UA and DA concentration is linearly dependent on the oxidation peak current over two ranges of low concentration (1 nM to 1 μM) and high concentration (10 μM - 1000 μM) with the R² > 0.9 in both the cases and its corresponding linear regression equations are given as follows Note S1.

Note S1: Linear regression equations for individual and simultaneous detection of DA and UA on NiCo₂O₄/CC.

1. Individual detection of DA and UA using SWV

a. For higher concentration region

$$I (\text{mA}/\text{cm}^2) = 3.15 + 1.20 \times 10^{-3} (\text{DA}; \mu\text{M}) (R^2 = 0.924) \text{ and} \quad (1)$$

$$I (\text{mA}/\text{cm}^2) = 4.09 + 9.22 \times 10^{-4} (\text{UA}; \mu\text{M}) (R^2 = 0.931). \quad (2)$$

b. For lower concentration region

$$I (\text{mA}/\text{cm}^2) = 0.39 + 2.25 (\text{DA}; \mu\text{M}) (R^2 = 0.984) \text{ and} \quad (3)$$

$$I (\text{mA}/\text{cm}^2) = 1.41 + 2.35 (\text{UA}; \mu\text{M}) (R^2 = 0.934). \quad (4)$$

2. Simultaneous detection of DA and UA

$$I (\text{mA}/\text{cm}^2) = 2.91 + 9.7 \times 10^{-4} (\text{DA}; \mu\text{M}) (R^2 = 0.971) \text{ and} \quad (5)$$

$$I (\text{mA}/\text{cm}^2) = 3.60 + 1 \times 10^{-3} (\text{UA}; \mu\text{M}) (R^2 = 0.945). \quad (6)$$

The NiCo₂O₄/CC possess a sensitivity of 2.25 mA.μM⁻¹cm⁻² in the lower region and 9.2 × 10⁻⁴ mA.μM⁻¹cm⁻² in the higher region for DA, while in the case of UA, it is found to be 2.35 mA.μM⁻¹cm⁻² and 1.2 × 10⁻³ mA.μM⁻¹cm⁻². The simultaneous detection was carefully tested by varying the concentration of the targeted bio-molecule while keeping the concentrations of the other biomolecule constant. When the concentration of UA (1 μM) was fixed, the current density of DA increased proportionally with the increasing DA concentration (Figure 6.9a). A similar trend was observed with increasing concentration of UA; the peak current density of UA increased gradually in the presence of DA (1 μM) (Figure 6.9b).

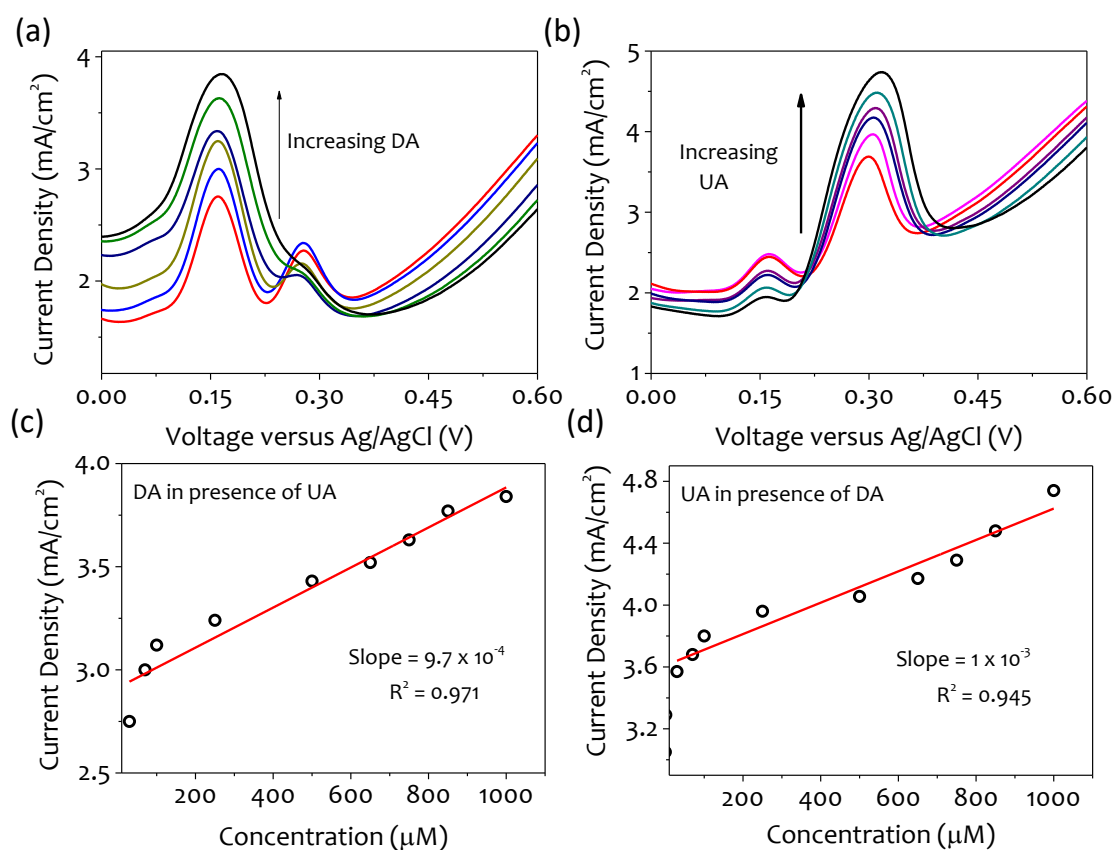


Figure 6.9: Simultaneous detection of (a) different concentrations of DA in the presence of 1 μM UA (b) different concentrations of UA in the presence of 1 μM DA and their corresponding (c-d) calibration plots.

The separation between the oxidation peaks was significant, which proves the possibility of simultaneous detection of DA and AA in a mixed solution. The slopes of the calibration plots obtained were almost similar to the individually detected DA and UA (Figure 6.9c and d). The simultaneous detection of DA and UA exhibited the sensitivity values of $1.67 \times 10^{-3} \text{ mA} \cdot \mu\text{M}^{-1} \text{ cm}^{-2}$ and $3 \times 10^{-3} \text{ mA} \cdot \mu\text{M}^{-1} \text{ cm}^{-2}$. The limit of detection (LOD) for DA in the lower and higher region was found to be 0.7 nM and 1.32 μM , and in the case of UA, it was 0.6 nM and 1.65 μM , respectively. The lower limit of detection in $\text{NiCo}_2\text{O}_4/\text{CC}$ can be attributed to the synergistic effect of the highly conducting NiCo_2O_4 nanoplates and higher adsorption sites provided by the 3D CC substrate for the oxidation of UA and DA biomolecules. As a sensor, $\text{NiCo}_2\text{O}_4/\text{CC}$ electrode must detect the concentration of these biomolecules in bodily fluid such as blood with UA in the range of 1–50 μM and DA of 0.01–1 μM . [Clark et al., 1997; Doménech et al., 2002] It is evident from the above values that the fabricated sensor can easily detect the biomolecules in bodily fluids.

However, it is also imperative for practical application to carry out measurements via easy techniques such as chronoamperometry methods. The $i-t$ responses of the $\text{NiCo}_2\text{O}_4/\text{CC}$ biosensor toward DA and UA are recorded at a slightly higher potential of 0.35 V and 0.45 V than the peak oxidation potential to obtain a significant response shown in Figure 6.10. The response current is measured under the optimized conditions at successive addition of DA or UA into the solution of 0.1 M PBS (pH=7). Figure 6.10a shows the $i-t$ measurement carried out for DA. The sudden spikes are seen with the addition of DA to the PBS due to changes in the mass transfer surrounding the electrode. The current response of DA increases linearly with increasing DA concentration in the two different linear ranges varying from 100 nM – 1 μM and 10 μM – 1000 μM (Figure 6.10a).

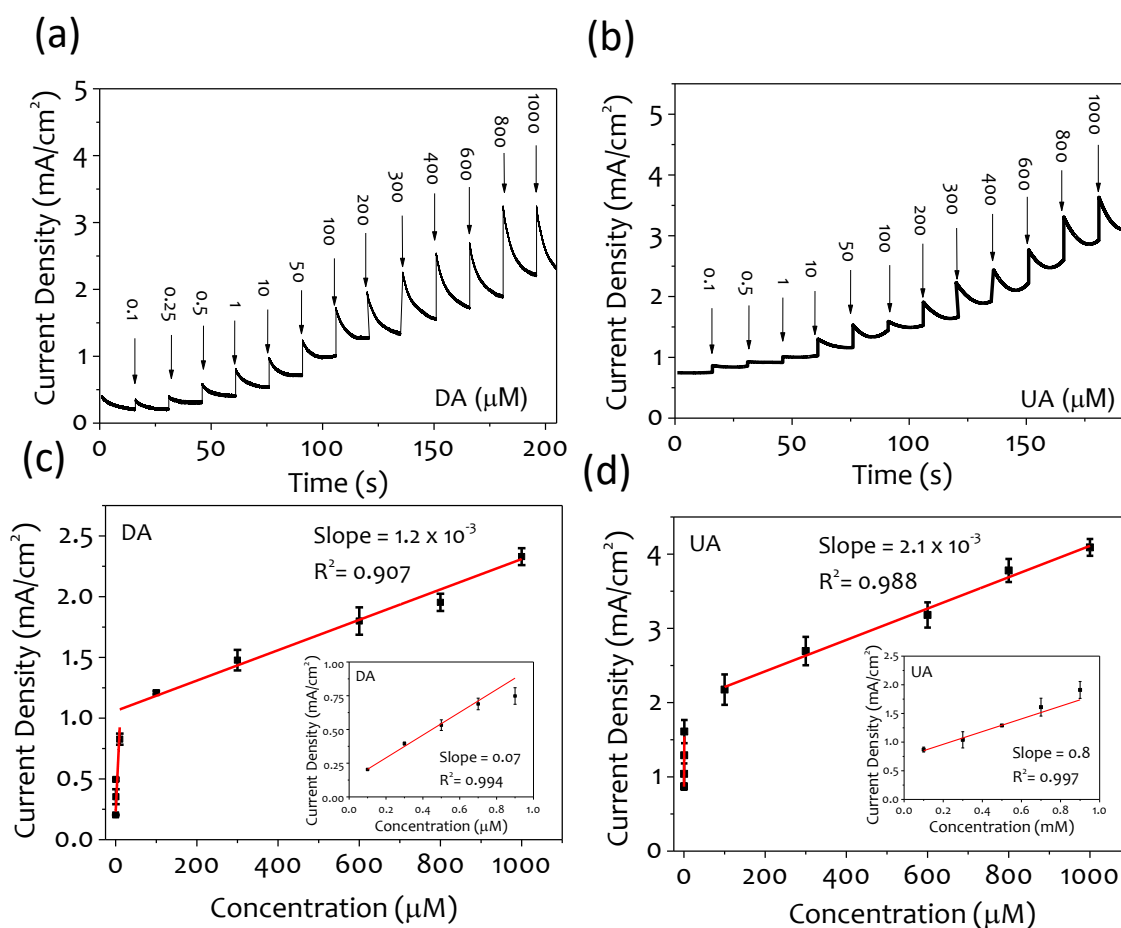


Figure 6.10: (a and b) Amperometric current (*i*-*t*) response with the increasing concentration of DA and UA at 0.35 V and 0.45 V, respectively, with insets showing a magnified view of the low concentration region. (c and d) Calibration plots derived from *i*-*t* measurements with error bars derived from repeat measurements.

Figure 6.10b illustrates the *i*-*t* of UA in which a similar trend of linear ranges is observed, which vary from 100 nM – 1 μ M and 10 μ M – 1000 μ M. In both cases, the $R^2 > 0.9$ and the lower detection limit of 1.9 nM and 22.5 nM are obtained from the calibration curve (lower region) at a signal-to-noise ratio of 3 for DA and UA, respectively (Figure 6.10c and d). A slight change in sensitivity values is observed compared to results obtained with SWV in both cases because of the change in the detection technique. The linear regression equations obtained from the calibration plots are as follows:

Individual detection of DA and UA using *i*-*t*

a. For higher concentration region

$$I \text{ (mA/cm}^2\text{)} = 1.05 + 1.20 \times 10^{-3} \text{ (DA; } \mu\text{M)} \text{ (} R^2 = 0.907\text{)} \text{ and} \quad (7)$$

$$I \text{ (mA/cm}^2\text{)} = 1.99 + 2.1 \times 10^{-3} \text{ (UA; } \mu\text{M)} \text{ (} R^2 = 0.995\text{)}. \quad (8)$$

b. For lower concentration region

$$I \text{ (mA/cm}^2\text{)} = 0.22 + 0.07 \text{ (DA; } \mu\text{M)} \text{ (} R^2 = 0.994\text{)} \text{ and} \quad (9)$$

$$I \text{ (mA/cm}^2\text{)} = 0.78 + 0.84 \text{ (UA; } \mu\text{M)} \text{ (} R^2 = 0.997\text{)}. \quad (10)$$

The lowest limit of quantification practically achievable using *i*-*t* measurements was found in the nM range for both UA and DA. Interestingly, the detection results are concomitant with the best values reported for other materials in literature and thus, guarantee a reliable biosensor

fabrication. The prepared NiCo_2O_4 demonstrates a wide linear range and relatively low detection limit. The strong sensing performance of the $\text{NiCo}_2\text{O}_4/\text{CC}$ electrode could be attributed to the nanoplate morphology that enables faster shuttling of ions and electrons at the electrode–electrolyte interface due to its crystalline nature and the presence of multiple oxidation cations (Ni and Co) on the surface, providing an ample number of active sites for oxidation of biomolecules.

6.4. Anti-Interference Studies

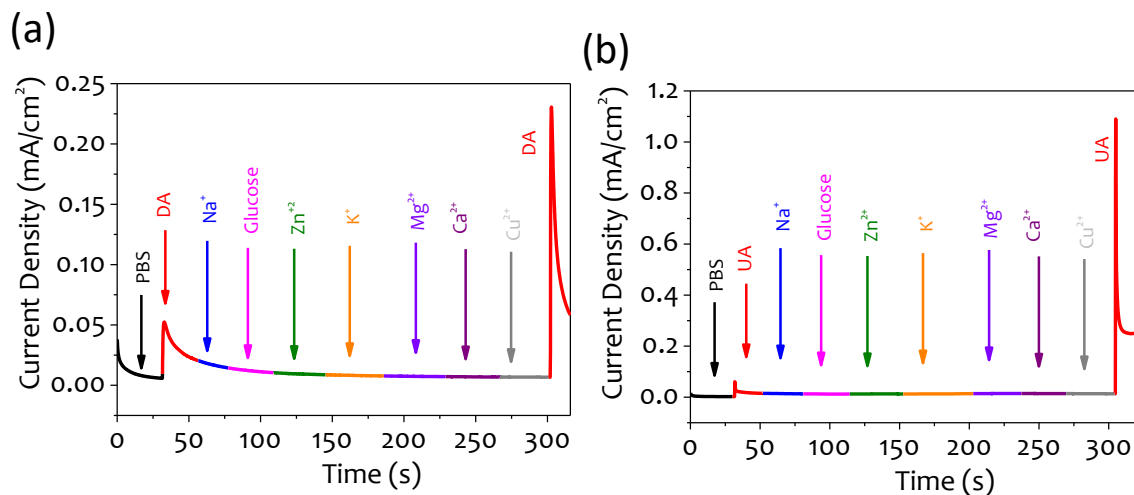


Figure 6.11 : Selectivity test of $\text{NiCo}_2\text{O}_4/\text{CC}$ electrode on successive addition of $5\ \mu\text{L}$ of Na^+ , glucose, Zn^{2+} , K^+ , Mg^{2+} , Ca^{2+} and Cu^{2+} ($1\ \text{mM}$) as interfering species to $0.1\ \text{M}$ solution of (a) DA and (b) UA in PBS at an applied potential of $0.35\ \text{V}$ and $0.45\ \text{V}$, respectively.

The selectivity of electrochemical DA and UA sensor is of high importance for practical application. Thus, the selectivity study was performed using Na^+ , Zn^{2+} , K^+ , Mg^{2+} , Ca^{2+} , Cu^{2+} , and glucose as interfering agents as their oxidation potentials could overlap with DA and UA, producing a false positive signal. Figures 6.11a and b show the amperometric response of the $\text{NiCo}_2\text{O}_4/\text{CC}$ electrode in Na^+ , Zn^{2+} , K^+ , Mg^{2+} , Ca^{2+} , Cu^{2+} ions, and glucose interfering agents along with DA and UA, respectively. Results show evident current changes upon DA and UA addition, respectively, with no or negligible current change upon the addition of other interfering species. The response for the DA and UA was observed instantaneously with a response time of less than seconds, which is comparatively faster than the reported values.[Jackowska et al., 2013; Xie et al., 2021] These interfering species do not cause any noticeable interference to the response of DA and UA, as displayed in Figures 6.11a and b, demonstrating an excellent selectivity and anti-interference ability of the NiCo_2O_4 biosensor toward the oxidation of DA and UA. These results conclude that NiCo_2O_4 can detect (DA and UA) individually and simultaneously over a wide linear range and even at low concentrations. The real-time sensing of bodily fluids with the possibility to determine the exact concentration of the UA and DA biomolecules in combination with various multivariate analysis techniques will be the future scope of the study.

6.5 Conclusions

In summary, we present a simple procedure for large-scale fabrication of NiCo_2O_4 nanoplates-based electrochemical biosensors to simultaneously detect DA and UA with high sensitivity. The $\text{NiCo}_2\text{O}_4/\text{CC}$ biosensor demonstrated excellent electrocatalytic performance, effective electron transfer capability, and high sensitivity compared with previously reported materials in the sensing of DA and UA. The strong sensing performance of the $\text{NiCo}_2\text{O}_4/\text{CC}$ electrode is because of the crystalline nanoplate morphology in synergy with the carbon cloth substrates

that enable faster shuttling of ions and electrons at the electrode–electrolyte interface and the presence of multiple Ni-Co cations on the surface, providing a large number of active sites which lowers the detection range and enhances the sensitivity. The perfect NiCo₂O₄/CC electrode achieves the simultaneous electrochemical determination of DA and UA with a wide linear concentration range of 0.001 – 1000 μM in both the cases and relatively better detection limits of 0.7 nM and 0.6 nM respectively. All of the features necessary for an electrocatalyst for sensing validate that the Ni-Co thiolate ink-based NiCo₂O₄ nanoplates electrode shows vast potential for multiple applications in biosensing technology.